ACS APPLIED MATERIALS & INTERFACES

Research Article

Cite This: ACS Appl. Mater. Interfaces 2018, 10, 25644−25651

www.acsami.org

Multifunctional Nanocracks in Silicon Nanomembranes by Notch-Assisted Transfer Printing

Yi Chen,[†,∥] Qinglei Guo,[†,∥] Gaoshan Huang,[†] Gongjin Li,[†] Lu Wang,[†] Ziao Tian,[†] Yuzhou Qin,[†] Zengfeng Di,[§] and Yongfeng Mei*[,†,‡]

[†]Department of Materials Science and [‡]State Key Laboratory of ASIC and Systems, Fudan University, Shanghai 200433, People's Republic of China

[§]State Key Laboratory of Functional Materials for Informatics, Shanghai Institute of Microsystem and Information Technology, Chinese Academy of Sciences, Shanghai 200050, People's Republic of China

Supporting Information

ABSTRACT: Manipulating nanocracks to produce various nanodevices has attracted increasing interest. Here, based on the mature transfer printing technique, a novel notch-assisted transfer printing technique was engaged to produce nanocracks by simply introducing notch structures into the transferred nanomembranes. Both experiments and finite element simulations were used to elucidate the probability of nanocrack formation during the transfer process, and the results demonstrated that the geometry of nanomembranes played a key role in concentrating stress and producing nanocracks. We further demonstrated that the obtained nanocrack can be used as a surface-enhanced Raman scattering substrate because of the significant enhancement of electric fields. In addition, the capillary condensation of water molecules in the nanocrack led to an obvious change of resistance, thus providing an opportunity for the crack-based structure to be used as an ultrasensitive humidity sensor. The current approach can be applied to producing nanocracks from multiple materials and will have important applications in the field of nanodevices.

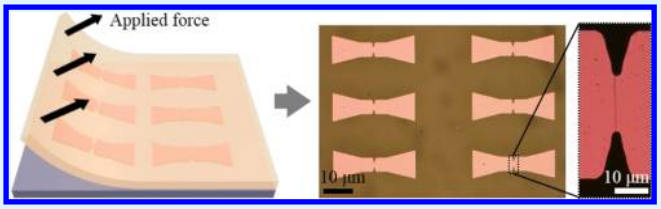

KEYWORDS: *nanocrack, transfer printing, notch, surface-enhanced Raman scattering, humidity sensing*

INTRODUCTION

Cracks are always considered as an unwanted material failure mode that should be avoided.[1] However, as a kind of micro-/nanostructure, cracks may also be engaged in producing structures with special features.[2−4] Recently, cracks with the size as low as sub-10 nm have been demonstrated,[3] which is comparable with the advanced e-beam lithography technology. Other advantages like facileness, low cost, and high throughput may also suggest their important potentials in the nanofabrication process.[5] Many methods of promoting crack initiation in different materials have been reported, including thermal cycling of multilayer samples with different thermal expansion coefficients,[6,7] swelling of polymer materials such as epoxy and SU-8 photoresist in solvents,[4,8] raising the stress between a deposited layer and the underlying material during the deposition of a thin brittle material,[3,5,9] applying uniform stress on polydimethylsiloxane (PDMS)-based materials,[10−14] and so forth. It is worth mentioning that these methods are all combined with the notch structures as stress raisers to manipulate the initiation and propagation of cracks.[15−19] These artificial cracks are applied in different fields: manipulating the morphology of cells,[10,11] detecting forces and sound,[14] as templates/molds for nanowires/nanochannels fabrication,[6−8,13,20] and integrating with ZnO nanoparticles to form ultraviolet photodetectors.[4] Despite the achievements in producing and manipulating cracks, there are still some limitations and drawbacks. In most cases, the individual approach only fits for a specific material. A universal crack fabrication and manipulation technique suitable for a wide range of materials is strongly required for practical applications.

Transfer printing is a versatile set of techniques of micro-/nanofabrication suitable for far-ranging classes of materials including hard materials, such as metals,[21−23] oxides,[24] and single-crystalline inorganic semiconductors.[25−28] The core of the technique is the use of a kinetically controlled adhesion of an elastomeric stamp (usually a PDMS rubber) to transfer printed solid objects from the donor substrate to the receiving substrate.[29,30] Inspired by the advantages of the widely applicable and controllable transfer printing technique, here we propose a notch-assisted transfer printing technique to produce nanocracks during the normal transfer printing process of a thin brittle nanomembrane by simply introducing notch structures into the nanomembrane as stress raisers. In this work, a controllable unidirectional nanocrack array was produced in a silicon nanomembrane (SiNM) and transferred readily onto a receiving substrate in a transfer printing process.

Received: April 28, 2018
Accepted: July 11, 2018
Published: July 11, 2018

DOI: 10.1021/acsami.8b06962
ACS Appl. Mater. Interfaces 2018, 10, 25644−25651

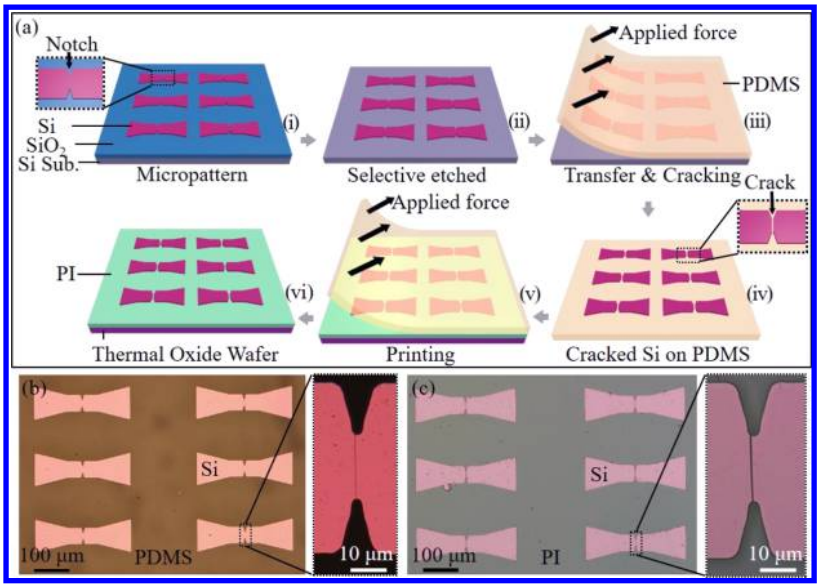

Figure 1. (a) Fabrication and transfer process of SiNMs with nanocrack structures by employing notch-assisted transfer printing technique. (b) Optical microscopy image of SiNMs with nanocrack structures on PDMS rubber fabricated by grabbing off SiNMs from the Si substrate through a peeling process. (c) Optical microscopy image of SiNMs with nanocrack structures transferred onto the receiving substrate PI.

Compared to the previously published work of preparing uniaxial metallic cracks on PDMS,[13] the current approach widens the material selection toward the single-crystalline silicon (and even other materials cannot be deposited on PDMS directly). As examples of practical applications, we demonstrate that the nanocrack can work as a surface-enhanced Raman spectroscopy (SERS) substrate with uniform enhancement and a humidity sensor with ultrahigh sensitivity. The present notch-assisted transfer printing technique is a promising nanofabrication technique that can be applied to multiple fields.

EXPERIMENTAL SECTION

Fabrication of Nanocracks. A silicon-on-insulator (SOI) wafer of (001) Si: 100 nm and SiO_2: 120 nm was used here. The top silicon layer of the SOI wafer was patterned with photolithography, followed by reactive ion etching (RIE) in SF_6: 15 sccm and O_2: 3 sccm at a pressure of 100 mTorr [Figure 1a-(i)]. Paired triangular notch structures working as stress raisers were designed in the micropattern. The connection lines of the paired notch vertexes were set to follow the <100> orientation to get straight cracks in the following process (see Figure S1 for more details).[5] Then, the wafer was cleaned and soaked in 30% HF solution for 6 h to remove the SiO_2 underlayer completely [Figure 1a-(ii)]. After that, a flat PDMS rubber (length: 2 cm; width: 1.5 cm; thickness: 0.2 cm) was attached to it intimately by the van der Waals force. The rubber was peeled away from the wafer quickly with a peeling velocity of about 10 cm/s to ensure the adhesion between the Si object array and the surface of PDMS [Figure 1a(iii)]. During the transfer process, the PDMS surface used for adhesion was expanded, thus generating a tensile strain in the brittle SiNM. When the induced tensile strain value exceeds the ultimate tensile strength (also called as fracture toughness), cracking fronts can be formed, which penetrate the SiNM and finally connect with each notch pair to produce nanocracks [Figure 1a-(iv)]. In the following step, the partially cured PI layer was used as the receiving substrate. Specifically, a three-step process was used to prepare the PI layer. PI2000 was first spin-coated on an oxide wafer at 4000 rpm for 30 s. Then, the sample was heated at 50 °C for 3 min and 150 °C for 5 min. To achieve the transfer process from PDMS to the PI substrate, PDMS and SiNM attached with the nanocrack structures were contacted to the receiving substrate PI manually. Pulling the PDMS rubber away from the PI substrate slowly with a peeling velocity of about 1 mm/s [Figure 1a-(v)] made the objects inclined to depart from PDMS and adhere to the receiving substrate, resulting in cracked SiNMs/PI devices [Figure 1a-(vi)]. The morphology of the nanocracks was characterized by scanning electron microscopy (SEM, Zeiss Sigma 300) and atomic force microscopy (AFM, Bruker Icon).

Influence from the Geometry of the Patterns. Micropatterns with various geometrical parameters (width, notch angle, and location of notches) were designed and fabricated. In this work, the width of the nanomembrane (d) was set as 20/30/40/60/100 μm, and the notch angle (θ) was set as 30°/60°/90°/120°/150°. The fracture probability at the notches in different patterns was calculated after the transfer printing process.

Theoretical Simulation. Simulation of the stress field distribution around the notch vertexes of different parameters during the transfer process was carried out via the finite element method (FEM). The idealized model consists of a PDMS rubber and a SiNM attached to the surface of PDMS. For the sake of clarity, the SiNM contained only one unpaired notch or one pair of notches in the model. The mechanical parameters of PDMS and SiNM were set according to the values reported in the literature,[31,32] and both Si and PDMS were set as linearly elastic materials. The length and width of PDMS in FEM are set as 300 and 200 μm, respectively. The thickness of SiNM was set as 0.1 μm. For the sake of simplicity, the thickness of PDMS was set as 50 μm, which is much larger than that of SiNM. To simulate the transfer process, one end of PDMS was fixed, whereas an ideal peeling force of 10^6 N/m^2 was applied on the edge near the opposite end with the direction perpendicular to the adhesion surface. SiNMs of different widths and notch angles were simulated.

SERS Measurements. A 30 nm thick Au layer was deposited on the cracked SiNM by electron beam evaporation to form a metallic nanogap. Then, 10^{-4} M rhodamine 6G (R6G) aqueous solution was dropped onto the gap. After 2 min, the extra solution was sopped up with a clean wiper. The sample was measured by a micro-Raman spectrometer (HORIBA LabRAM XploRA Plus) with a 532 nm laser as an excitation source. The laser was focused on the sample via a 100× lens, and the spot was about 1.5 μm in diameter. The laser power was 0.05 mW. The exposure time was kept as 1 s.

Humidity Sensing. The n-type SiNMs with a low resistivity of 0.03 Ω·cm (phosphorus doping concentration: ~10^{19} cm^{-3}) was used in this experiment, and two-terminal devices were produced by depositing gold electrodes on the cracked SiNM/PI structures. Two nanocracks with widths of 40 and 400 nm were tested (see Figure S2 for the method of controlling the crack width). The alterable relative

DOI: 10.1021/acsami.8b06962
ACS Appl. Mater. Interfaces 2018, 10, 25644−25651

humidity (RH) for the tests was generated by saturated salt (K_2CO_3, NaCl, and K_2SO_4) solutions, and the corresponding RH values were 43, 75, and 98%, respectively, at 20 °C and 1 atm. The electrical measurements were carried out on a semiconductor parameter analyzer (Keithley 4200).

RESULTS AND DISCUSSION

The fabrication process of the nanocrack structures is shown in the flowchart in Figure 1a. The micropattern was designed with paired notches whose vertexes were capable of concentrating stress.[15−18] The vertexes were more likely to reach the ultimate tensile strength and become the initiation points of the cracks. The SOI wafer was patterned with a photoresist by standard photolithography, and then the exposed silicon was etched away by RIE. After removing the photoresist, the wafer was immersed in HF solution to etch the underneath SiO_2 layer. The released SiNM was attached to the substrate via the van der Waals force during the slow etching process. Then, a flat PDMS rubber was contacted to the wafer intimately and peeled back quickly along the direction perpendicular to the connection line between the vertexes of the paired notches. At a fast peeling rate, the adhesion between the PDMS rubber and the SiNMs was much stronger than that between the SiNMs and the Si substrate,[30] and the patterned SiNMs were grabbed off from the donor substrate. During the peeling process, PDMS was bent and the SiNMs were also stretched. Once the stress of the notch vertex reached the ultimate tensile strength, cracks would appear instantly,[33] connecting the paired notches horizontally and penetrating the SiNMs in the vertical direction. The PDMS rubber and the SiNMs attached with the nanocrack structures were then printed onto a receiving substrate, that is, PI spin-coated on a thermally oxidized Si substrate. Here, PI was selected as the adhesion layer because of its thermal stability, good chemical resistance, and excellent mechanical properties.[34] Finally, the PDMS rubber was peeled back slowly. In this case, the adhesion between Si and PDMS became weaker than the interaction between Si and PI,[30] and the SiNMs with nanocrack structures were transferred to the PI surface. Figure 1b displays an optical photograph of a typical as-fabricated cracked SiNM array on PDMS and an enlarged image of a nanocrack structure, which demonstrates that the width of the crack is in nanometer scale. There was no visible deformation in the SiNMs around the cracked area, indicating that the deformation energy was concentrated at the locations of the crack.[35] Figure 1c presents the same cracked SiNM array as that shown in Figure 1b transferred onto the receiving substrate PI. The nanocrack structure keeps its original morphology well with only a slight broadening of width (but still within the nanometer size). A further morphological characterization of nanocracks by AFM can be found in Figure S3.

The above method of fabricating nanocrack structures is a facile and low-cost strategy to produce unidirectional nanostructures, and it is also compatible with the widely used transfer printing techniques, which means a potential application of integration with various function systems like flexible electronics[36,37] and optoelectronics.[38−43] The effect of various parameters on the cracking process of SiNMs will be discussed in the following section.

To improve the fracture probability of SiNMs during the transfer process, the stress concentrated at the notch vertexes was increased by adjusting the geometrical parameters of the notch structures. Figure 2a presents three parameters we have investigated: notch angle (θ), width of SiNMs (d), and paired/unpaired notches. Here, the notch angle θ was set as 30°/60°/90°/120°/150°, and the width d was set as 20/30/40/60/100 μm. The values of θ and d of SiNMs in Figure 2a were 90° and 30 μm, respectively. In the present work, the bottom length of the notches and the spacing between the neighboring notches were kept constant at 10 and 50 μm, respectively. In addition, the patterned SiNMs with notches at a single side were compared with those with paired notches. For the SiNMs with unpaired notches, cracks initiated from the notches and terminated at the opposite side. For the SiNMs with paired notches, the cracks connected the notches.[8,19] We prepared patterned SiNMs with different geometries and studied their influence on fracture probability. In each case, more than 100 notches that transferred simultaneously onto the same PDMS were counted, and the statistics are shown in Figure 2b,c. Figure 2b shows the proportion of cracks under different θ and at the same d of 20 μm. The statistical result indicates that the probability of crack formation decreases with an increase of θ, meaning that the stress can be hardly concentrated at large θ. The probability in the case of unpaired notches comes to about 100% when θ = 30°, whereas the probability for paired notches reaches 100% when θ = 60°. This indicates that the probability of crack formation in SiNMs with paired notches is always higher than that with unpaired notches. Figure 2c displays the

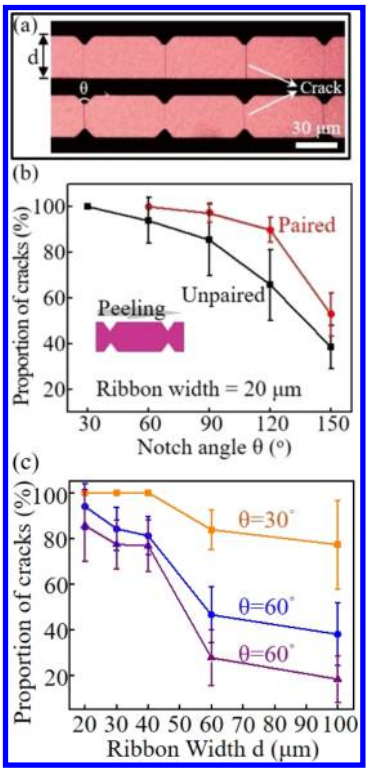

Figure 2. Influence of geometrical parameters of notches on the proportion of cracks in transferred SiNMs. (a) Optical microscopy image of cracked SiNMs with unpaired/paired notches on PDMS. The notch angle θ and the width d are labeled. (b) Statistical results of the proportion of cracks in transferred SiNMs with paired/unpaired notches. The value of θ increases from 30° to 150° with a step of 30°, and d is kept constant at 20 μm. (c) Statistical results of the proportion of cracks in transferred SiNMs with unpaired notches. The value of d is set as 20/30/40/60/100 μm.

DOI: 10.1021/acsami.8b06962
ACS Appl. Mater. Interfaces 2018, 10, 25644−25651

relationship between d and the proportion of cracks in the case of unpaired notches. At $\theta = 30°$, the change of width from 20 to 40 μm has no effect on the probability, indicating that sharp notches can strongly concentrate stress. However, as the width increases further, the fracture probability starts to decrease. For notches with larger angles, that is, $\theta = 60°$ or 90°, the probability is less than 100% and decreases obviously with d. The above results reflect a downtrend of stress evolution at the location of the vertexes as the width increases.

According to the maximum normal stress strength theory, brittle materials break once the stress reaches the ultimate tensile strength. Here, the simulations of stress distributions in SiNMs with different geometries (i.e., different d and θ), before the initiation of cracks, are carried out by FEM. The model is shown in Figure 3a. Because the interaction between

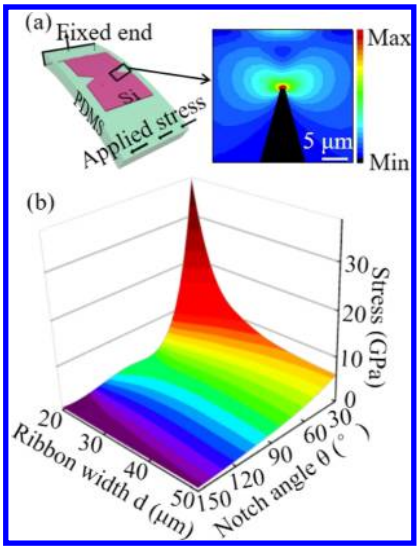

Figure 3. (a) Left: theoretical model of the transfer process. Right: calculated stress distribution at the vicinity of the notch ($\theta = 30°$) vertex before the crack initiation. (b) Calculated maximum stress at the notch vertex as a function of notch angle θ and the SiNM width d. The applied stress at the end is kept at 10^6 N/m^2.

PDMS and SiNMs is much stronger than that of SiNMs and the Si substrate during the faster peeling process,[30] the model only consists of a PDMS rubber and a SiNM stacking on the surface of PDMS, and the SiNM contains only one pair of notches (simulation of an unpaired notch is presented in Figure S4.). PDMS is set as a linearly elastic material because of its high elasticity, small bending amplitude, and small deformation time.[31] Si is also set as a linearly elastic material without ductility at room temperature.[44] Here, the thickness of PDMS was set as 50 μm, which is much larger than that of SiNM. The deviation between the simulation and experiment can be neglected, as the bending status of the PDMS substrate determines the stress in the SiNM. In the simulation, one end of PDMS is fixed, whereas an ideal peeling force of 10^6 N/m^2 (according to our experiment) is applied on the opposite end with the direction perpendicular to the adhesion surface. The right panel of Figure 3a displays the simulated stress distribution around a notch with $\theta = 30°$. Stress is concentrated at the notch vertex, indicating that the stress at the vicinity of the vertex is most likely to reach the ultimate tensile strength and causes the initiation of crack. The stress at other places is significantly smaller than that at the vertex, such that unintentional cracks can hardly be observed. Figure 3b shows the dependencies of the maximum stress at the vicinity of the vertex on d and θ. At the same d, the stress decreases obviously with an increase of θ, which fits well with the experimental results shown in Figure 2b. At the same θ, the stress decreases quickly with an increase of d if the notch is very sharp. However, the decrease becomes relatively inconspicuous for larger θ (see Figure 3b). Further, the stresses in the cases of small θ are always higher than larger θ, and thus the proportion of cracks should increase correspondingly, as experimentally observed in Figure 2c.

SERS is of great interest because of its ability of manipulating and detecting materials from very small volumes (minimum to molecular scale),[45−47] and it can save cost and ensure repeatability of measurement.[48−50] Gold is frequently chosen in SERS because of its localized surface plasmons (LSPs).[9,51,52] Among plasmonic devices, nanogaps based on metal−insulator−metal (Au−air−Au) structures have been investigated deeply because of the significant enhancement of the electric fields.[53−55] Here, we demonstrated that an Au-coated nanocrack has uniform Raman enhancement. In our experiment, a 30 nm thick Au layer was deposited on the cracked SiNMs/PDMS sample at a very low rate to ensure a uniform coating layer and form a metallic nanogap (width: 150 nm). Figure 4a shows the SEM image of the Au-coated

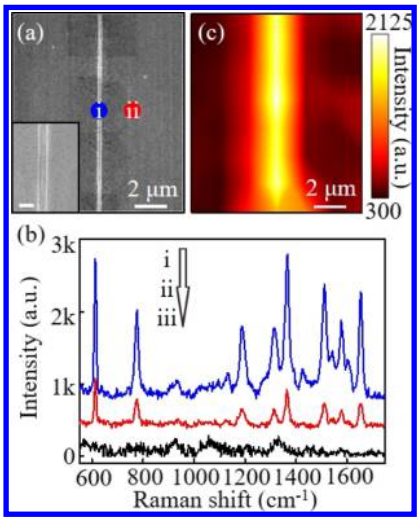

Figure 4. (a) SEM image of an Au-coated cracked SiNM on PDMS. The inset is the enlarged image, and the scale bar is 200 nm. (b) Comparison of SERS spectra collected from different locations: (i) nanogap structure; (ii) 2 μm away from the gap; (iii) surface of cracked SiNMs without an Au coating on PDMS. (c) Raman intensity map of the characteristic peak of 1362 cm^{-1} at the vicinity of the nanogap.

nanocrack. In the current SERS characterization, the probe molecule used is R6G, and the Au surface is capable of absorbing R6G molecules by an electrostatic force and N−Au interaction.[56,57] Figure 4b presents the typical Raman spectra of R6G collected from different locations around the nanocrack and on bare SiNM. The blue line (plot i) displays the spectrum collected from the center of the gap (see Figure 4a). The red line (plot ii) represents the Raman signal of a spot on the Au substrate 2 μm away from the gap (see Figure 4a). For comparison, the black line (plot iii) exhibits the Raman signal from R6G molecules on a cracked SiNMs/PDMS

DOI: 10.1021/acsami.8b06962
ACS Appl. Mater. Interfaces 2018, 10, 25644−25651

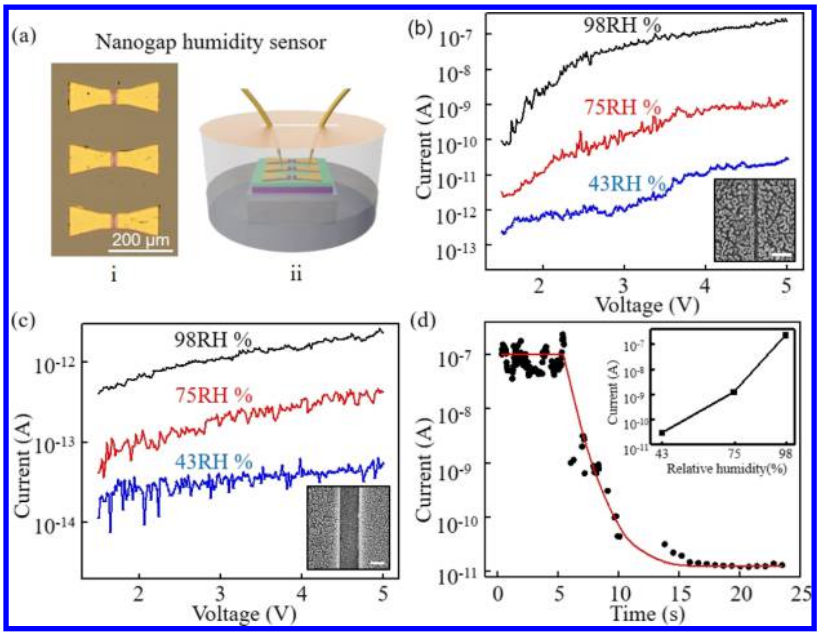

Figure 5. (a-i) Optical microscopy image of the humidity sensors: cracked SiNMs transferred onto PI with a pair of Au electrodes deposited on them. (a-ii) Experimental configuration for electrical measurements. (b,c) Typical $I-V$ curves of two sensors in different RHs at 20 °C and 1 atm. The insets are the SEM images of the corresponding nanocrack structures. Both scale bars are 300 nm. (d) Response of the sensor device shown in figure 5b. RH is decreased from 98 to 43%. The red line is a guide to the eye. The inset shows the current at different RHs when the applied voltage is 5 V.

without an Au coating layer (see Figure S5 for more details). An obvious enhancement in plots (i and ii) can be observed, whereas no Raman signal can be detected in plot (iii). The two spectra (i and ii) show the characteristic peaks of R6G, that is, 1362, 1507, and 1650 cm^{-1}, which are attributed to the totally symmetric modes of the in-plane C−C stretching vibration.[58] It is worth noting that the intensity of plot (i) is about 4 times larger than that of plot (ii) (see also the Supporting Information). We also experimentally noticed that the intensity of Raman signal decreased rapidly at the spots away from the nanogap and tended to be constant at a flat region without gap. To demonstrate this feature clearly, we carried out Raman mapping measurement on the sample. Figure 4c shows the Raman mapping results with an area of 14 × 12 μm^2, where the intensity of the peak at 1362 cm^{-1} is traced. Throughout the 14 μm length of the nanogap, Raman signal enhancement is quite uniform.

According to previous literature, the mechanism of Raman signal enhancement in a nanogap can be attributed to LSPs at the bottom of the nanogap[55] and/or the metal−insulator−metal symmetric surface plasmon polariton modes.[59] The uniform enhancement in Figure 4c indicates that the nanocrack has an even width, as the nanogap's electrical field enhancement value is sensitive to its width.[59] The well-behaved Raman enhancement of the Au-coated nanocrack implies its potential of working as an excellent and inexpensive SERS substrate in the bioanalysis field.

The demand of monitoring and controlling water vapor content in various environments requires fast-reacting, sensitive, and reliable humidity sensors. Previously, Si-based materials, like porous silicon, have been made into numerous structures to measure humidity and showed good performance.[60−62] Here, we demonstrated that the cracked SiNMs can be engaged as humidity sensors with ultrahigh sensitivity and fast response. Figure 5a-(i),a-(ii) presents the sensor device and experimental configuration used in our experiment (see Figure S6 for more details). RHs in the chamber were stabilized at 98, 75, and 43%. The device is actually an electronic nanogap with a high resistance. Here, the SiNMs with high doping concentration and low resistivity were used to reduce the resistance of the SiNM and thus highlight the resistance variation of the nanogap. When the device was placed in environments with water vapor, the adsorbed water molecules in the gap formed a liquid bridge[63] that connected the two parts of the crack and provided a channel for charge transportation, leading to resistance decrease of the device. An increase in the RH level led to increased moisture adsorption, resulting in increased water molecules, heterogeneous nucleation rate, and condensation volume,[64] and thus an increase in the current. Figure 5b presents the $I-V$ curve of an as-fabricated sensor device, with the nanocrack width of about 40 nm (as displayed in the inset), at different RHs, where the voltage is in the range of 1.5−5 V. An obvious evolution of the current in an environment with different RHs is noticeable. At a voltage of 5 V, for example, when RH is raised from 43 to 98%, the measured current increased by about 4 orders of magnitude. The $I-V$ curves of a sensor device with the nanocrack width of about 400 nm at different RHs are presented in Figure 5c, which shows much smaller currents at the same RH condition compared to those in Figure 5b. At 5 V, the current increases by only 2 orders of magnitude when RH is raised from 43 to 98%. One can see that both devices are sensitive to RH in the environment. The current difference between the two devices (Figure 5b,c) under the same external conditions is considered to be geometry related because the width of the nanocrack influenced the capillary nucleation of the water molecules.[65−68] Capillary nucleation and the following condensation are remarkable in the nanoscale-confined space as the introduction of boundary conditions reduces the mean free path of gas molecules and increases their

DOI: 10.1021/acsami.8b06962
ACS Appl. Mater. Interfaces 2018, 10, 25644−25651

interaction probability. The characteristic length for the water vapor molecules is about 128 nm at the experimental conditions of 293 K and 1 atm (see the Supporting Information for detailed calculation). Hence, the 40 nm wide nanocrack in Figure 5b leads to strong condensation of water molecules, whereas in the case of 400 nm wide nanocrack, the above effect should not be predominant. As a result, the current evolution in the case of 40 nm wide nanocrack is much higher, as shown in Figure 5. We should also stress that the sensitivity for the present device made from an individual narrow nanocrack is obviously higher than that from a wider crack or multiple cracks.[69] Moreover, to test the response time of the sensor with a narrower crack (width: 40 nm), RH was lowered from 98 to 43% by rapidly replacing the corresponding saturated solution, whereas the voltage was held at 5 V. Figure 5d shows the corresponding $I-t$ curve, and $t = 0$ represents the time point when the fluid was totally replaced. It took about 10 s for the current to drop from 10^{-7} to 10^{-11} A and become stable. The stable current values at high and low RHs are consistent with the values in Figure 5b at 5 V and different RHs (see the inset of Figure 5d). This response time (~10 s) is several times smaller than that of many reported humidity sensors.[70]

CONCLUSIONS

In summary, unidirectional nanocracks in thin brittle SiNMs have been achieved by employing the proposed notch-assisted transfer printing process as well as their transfer onto the receiving substrate PI. Geometrical parameters play a key role in nanocrack formation: the sharper the angle, the narrower the width, the larger the stress concentrated at the notch vertex, which leads to higher nanocrack initiation probability. We have demonstrated the nanocrack structure's excellent abilities in the field of SERS and humidity sensing. SERS measurements provide a very uniform intensity enhancement along the nanocrack, whereas humidity sensing displays ultrahigh sensitivity and fast-response ability because of capillary nucleation and condensation in the confined space of the nanocrack. Our research provides a universal, facile, inexpensive, and high-precision candidate technique of nanofabrication, which can be applied to various transferable materials for different functions.

ASSOCIATED CONTENT

Supporting Information

The Supporting Information is available free of charge on the ACS Publications website at DOI: 10.1021/acsami.8b06962.

SERS measurements of reference samples; SERS enhancement factor calculation; optical images of fabrication process of humidity sensors; andcalculation of mean free path of water molecules (PDF)

AUTHOR INFORMATION

Corresponding Author

*E-mail: yfm@fudan.edu.cn.

ORCID

Gaoshan Huang: 0000-0002-0525-7177

Zengfeng Di: 0000-0002-9357-5107

Yongfeng Mei: 0000-0002-3314-6108

Author Contributions

‖Y.C. and Q.G. contributed equally to this work.

Notes

The authors declare no competing financial interest.

ACKNOWLEDGMENTS

This work is supported by the Natural Science Foundation of China (51711540298, 61628401, U1632115, 51602056), Science and Technology Commission of Shanghai Municipality (17JC1401700), the National Key Technologies R&D Program of China (2015ZX02102-003), and the Changjiang Young Scholars Program of China. Q.L.G. acknowledges China Postdoctoral Science Foundation no. 2015M581523 and the International Postdoctoral Exchange Fellowship Program supported by the Office of China Postdoctoral Council.

REFERENCES

(1) Koyama, M.; Zhang, Z.; Wang, M.; Ponge, D.; Raabe, D.; Tsuzaki, K.; Noguchi, H.; Tasan, C. C. Bone-like Crack Resistance in Hierarchical Metastable Nanolaminate Steels. *Science* **2017**, *355*, 1055−1057.

(2) Kim, M.; Kim, D.-J.; Ha, D.; Kim, T. Cracking-assisted Fabrication of Nanoscale Patterns for Micro/nanotechnological Applications. *Nanoscale* **2016**, *8*, 9461−9479.

(3) Dubois, V.; Niklaus, F.; Stemme, G. Crack-Defined Electronic Nanogaps. *Adv. Mater.* **2016**, *28*, 2178−2182.

(4) Zhao, Q.; Wang, W.; Shao, J.; Li, X.; Tian, H.; Liu, L.; Mei, X.; Ding, Y.; Lu, B. Nanoscale Electrodes for Flexible Electronics by Swelling Controlled Cracking. *Adv. Mater.* **2016**, *28*, 6337−6344.

(5) Nam, K. H.; Park, I. H.; Ko, S. H. Patterning by Controlled Cracking. *Nature* **2012**, *485*, 221−224.

(6) Sardan, O.; Yalcinkaya, A. D.; Alaca, B. E. Self-assembly-based batch fabrication of nickel-iron nanowires by electroplating. *Nanotechnology* **2006**, *17*, 2227−2233.

(7) Jebril, S.; Elbahri, M.; Titazu, G.; Subannajui, K.; Essa, S.; Niebelschütz, F.; Röhlig, C.-C.; Cimalla, V.; Ambacher, O.; Schmidt, B.; Kabiraj, D.; Avasti, D.; Adelung, R. Integration of Thin-film-fracture-based Nanowires into Microchip Fabrication. *Small* **2008**, *4*, 2214−2221.

(8) Kim, M.; Ha, D.; Kim, T. Cracking-assisted Photolithography for Mixed-scale Patterning and Nanofluidic Applications. *Nat. Commun.* **2015**, *6*, 6247.

(9) Alaca, B. E.; Sehitoglu, H.; Saif, T. Guided Self-assembly of Metallic Nanowires and Channels. *Appl. Phys. Lett.* **2004**, *84*, 4669−4671.

(10) Zhu, X.; Mills, K. L.; Peters, P. R.; Bahng, J. H.; Liu, E. H.; Shim, J.; Naruse, K.; Csete, M. E.; Thouless, M. D.; Takayama, S. Fabrication of Reconfigurable Protein Matrices by Cracking. *Nat. Mater.* **2005**, *4*, 403−406.

(11) Kim, B. C.; Moraes, C.; Huang, J.; Matsuoka, T.; Thouless, M. D.; Takayama, S. Fracture-based Fabrication of Normally Closed, Adjustable, and Fully Reversible Microscale Fluidic Channels. *Small* **2014**, *10*, 4020−4029.

(12) Kim, B. C.; Matsuoka, T.; Moraes, C.; Huang, J.; Thouless, M. D.; Takayama, S. Guided Fracture of Films on Soft Substrates to Create Micro/nano-feature Arrays with Controlled Periodicity. *Sci. Rep.* **2013**, *3*, 3027.

(13) Huh, D.; Mills, K. L.; Zhu, X.; Burns, M. A.; Thouless, M. D.; Takayama, S. Tuneable Elastomeric Nanochannels for Nanofluidic Manipulation. *Nat. Mater.* **2007**, *6*, 424−428.

(14) Kang, D.; Pikhitsa, P. V.; Choi, Y. W.; Lee, C.; Shin, S. S.; Piao, L.; Park, B.; Suh, K.-Y.; Kim, T.-i.; Choi, M. Ultrasensitive Mechanical Crack-based Sensor Inspired by the Spider Sensory System. *Nature* **2014**, *516*, 222−226.

(15) Atzori, B.; Lazzarin, P.; Filippi, S. Cracks and Notches: Analogies and Differences of the Relevant Stress Distributions and Practical Consequences in Fatigue Limit Predictions. *Int. J. Fatigue* **2001**, *23*, 355−362.

DOI: 10.1021/acsami.8b06962
ACS Appl. Mater. Interfaces 2018, 10, 25644−25651

(16) Filippi, S.; Lazzarin, P.; Tovo, R. Developments of Some Explicit Formulas Useful to Describe Elastic Stress Fields Ahead of Notches in Plates. *Int. J. Solids Struct.* **2002**, *39*, 4543−4565.
(17) Filippi, S. Distributions of the Elastic Principal Stress Due to Notches in Finite Size Plates and Rounded Bars Uniaxially Loaded. *Int. J. Fatigue* **2004**, *26*, 377−391.
(18) Lazzarin, P.; Filippi, S. A Generalized Stress Intensity Factor to be Applied to Rounded V-shaped Notches. *Int. J. Solids Struct.* **2006**, *43*, 2461−2478.
(19) Erdem Alaca, B.; Ozcan, C.; Anlas, G. Deterministic Assembly of Channeling Cracks as A Tool for Nanofabrication. *Nanotechnology* **2010**, *21*, 055301.
(20) Kim, M.; Kim, T. Crack-Photolithography for Membrane-Free Diffusion-Based Micro/Nanofluidic Devices. *Anal. Chem.* **2015**, *87*, 11215−11223.
(21) Smythe, E. J.; Dickey, M. D.; Whitesides, G. M.; Capasso, F. A Technique to Transfer Metallic Nanoscale Patterns to Small and Non-Planar Surfaces. *ACS Nano* **2009**, *3*, 59−65.
(22) Schmid, H.; Wolf, H.; Allenspach, R.; Riel, H.; Karg, S.; Michel, B.; Delamarche, E. Preparation of Metallic Films on Elastomeric Stamps and Their Application for Contact Processing and Contact Printing. *Adv. Funct. Mater.* **2003**, *13*, 145−153.
(23) Loo, Y.-L.; Willett, R. L.; Baldwin, K. W.; Rogers, J. A. Interfacial Chemistries for Nanoscale Transfer Printing. *J. Am. Chem. Soc.* **2002**, *124*, 7654−7655.
(24) Kim, T.-H.; Choi, W. M.; Kim, D.-H.; Meitl, M. A.; Menard, E.; Jiang, H.; Carlisle, J. A.; Rogers, J. A. Printable, Flexible, and Stretchable Forms of Ultrananocrystalline Diamond with Applications in Thermal Management. *Adv. Mater.* **2008**, *20*, 2171−2176.
(25) Baca, A. J.; Ahn, J.-H.; Sun, Y.; Meitl, M. A.; Menard, E.; Kim, H.-S.; Choi, W. M.; Kim, D.-H.; Huang, Y.; Rogers, J. A. Semiconductor Wires and Ribbons for High Performance Flexible Electronics. *Angew. Chem., Int. Ed. Engl.* **2008**, *47*, 5524−5542.
(26) Guo, Q.; Zhang, M.; Xue, Z.; Wang, G.; Chen, D.; Cao, R.; Huang, G.; Mei, Y.; Di, Z.; Wang, X. Deterministic Assembly of Flexible Si/Ge Nanoribbons via Edge-Cutting Transfer and Printing for Van Der Waals Heterojunctions. *Small* **2015**, *11*, 4140−4148.
(27) Guo, Q.; Di, Z.; Lagally, M. G.; Mei, Y. Strain engineering and mechanical assembly of silicon/germanium nanomembranes. *Mater. Sci. Eng., R* **2018**, *128*, 1−31.
(28) Sun, Y.; Rogers, J. A. Inorganic Semiconductors for Flexible Electronics. *Adv. Mater.* **2007**, *19*, 1897−1916.
(29) Carlson, A.; Bowen, A. M.; Huang, Y.; Nuzzo, R. G.; Rogers, J. A. Transfer Printing Techniques for Materials Assembly and Micro/nanodevice Fabrication. *Adv. Mater.* **2012**, *24*, 5284−5318.
(30) Meitl, M. A.; Zhu, Z.-T.; Kumar, V.; Lee, K. J.; Feng, X.; Huang, Y. Y.; Adesida, I.; Nuzzo, R. G.; Rogers, J. A. Transfer Printing by Kinetic Control of Adhesion to An Elastomeric Stamp. *Nat. Mater.* **2005**, *5*, 33−38.
(31) Lötters, J. C.; Olthuis, W.; Veltink, P. H.; Bergveld, P. The Mechanical Properties of the Rubber Elastic Polymer Polydimethylsiloxane for Sensor Applications. *J. Micromech. Microeng.* **1997**, *7*, 145−147.
(32) Kim, M. T. Influence of Substrates on the Elastic Reaction of Films for the Microindentation Tests. *Thin Solid Films* **1996**, *283*, 12−16.
(33) Hauch, J. A.; Holland, D.; Marder, M. P.; Swinney, H. L. Dynamic Fracture in Single Crystal Silicon. *Phys. Rev. Lett.* **1999**, *82*, 3823−3826.
(34) Liaw, D.-J.; Wang, K.-L.; Huang, Y.-C.; Lee, K.-R.; Lai, J.-Y.; Ha, C.-S. Advanced Polyimide Materials: Syntheses, Physical Properties and Applications. *Prog. Polym. Sci.* **2012**, *37*, 907−974.
(35) Gross, D.; Seelig, T. *Fracture Mechanics with an Introduction to Micromechanics*, 1st ed.; Springer Publications: Berlin, Heidelberg, 2006.
(36) Kim, S.; Jeong, H. Y.; Kim, S. K.; Choi, S.-Y.; Lee, K. J. Flexible Memristive Memory Array on Plastic Substrates. *Nano Lett.* **2011**, *11*, 5438−5442.
(37) Sekitani, T.; Zschieschang, U.; Klauk, H.; Someya, T. Flexible Organic Transistors and Circuits with Extreme Bending Stability. *Nat. Mater.* **2010**, *9*, 1015−1022.
(38) Song, E.; Guo, Q.; Huang, G.; Jia, B.; Mei, Y. Bendable Photodetector on Fibers Wrapped with Flexible Ultrathin Single Crystalline Silicon Nanomembranes. *ACS Appl. Mater. Interfaces* **2017**, *9*, 12171−12175.
(39) Seo, J.-H.; Zhang, K.; Kim, M.; Zhao, D.; Yang, H.; Zhou, W.; Ma, Z. Flexible Phototransistors Based on Single-Crystalline Silicon Nanomembranes. *Adv. Opt. Mater.* **2016**, *4*, 120−125.
(40) Kim, M.; Seo, J.-H.; Yu, Z.; Zhou, W.; Ma, Z. Flexible germanium nanomembrane metal-semiconductor-metal photodiodes. *Appl. Phys. Lett.* **2016**, *109*, 051105.
(41) Dang, M.; Yuan, H.-C.; Ma, Z.; Ma, J.; Qin, G. The fabrication and characterization of flexible single-crystalline silicon and germanium p-intrinsic-n photodetectors on plastic substrates. *Appl. Phys. Lett.* **2017**, *110*, 253104.
(42) Kim, M.; Liu, S.-C.; Kim, T. J.; Lee, J.; Seo, J.-H.; Zhou, W.; Ma, Z. Light absorption enhancement in Ge nanomembrane and its optoelectronic application. *Opt. Express* **2016**, *24*, 16894−16903.
(43) Dang, M.; Yuan, H.-C.; Ma, Z.; Ma, J.; Qin, G. The Fabrication and Characterization of Flexible Single-crystalline Silicon and Germanium P-intrinsic-n Photodetectors on Plastic Substrates. *Appl. Phys. Lett.* **2017**, *110*, 253104.
(44) Schneider, F.; Fellner, T.; Wilde, J.; Wallrabe, U. Mechanical Properties of Silicones for MEMS. *J. Micromech. Microeng.* **2008**, *18*, 065008.
(45) Hu, M.; Ou, F. S.; Wu, W.; Naumov, I.; Li, X.; Bratkovsky, A. M.; Williams, R. S.; Li, Z. Gold Nanofingers for Molecule Trapping and Detection. *J. Am. Chem. Soc.* **2010**, *132*, 12820−12822.
(46) Lin, E.-C.; Fang, J.; Park, S.-C.; Johnson, F. W.; Jacobs, H. O. Effective Localized Collection and Identification of Airborne Species Through Electrodynamic Precipitation and SERS-based Detection. *Nat. Commun.* **2013**, *4*, 1636.
(47) Wang, C.; Yu, C. Analytical Characterization Using Surface-enhanced Raman Scattering (SERS) and Microfluidic Sampling. *Nanotechnology* **2015**, *26*, 092001.
(48) Kayani, A. A.; Khoshmanesh, K.; Ward, S. A.; Mitchell, A.; Kalantar-zadeh, K. Optofluidics Incorporating Actively Controlled Micro- and Nano-particles. *Biomicrofluidics* **2012**, *6*, 031501.
(49) Chrimes, A. F.; Khoshmanesh, K.; Stoddart, P. R.; Mitchell, A.; Kalantar-zadeh, K. Microfluidics and Raman Microscopy: Current Applications and Future Challenges. *Chem. Soc. Rev.* **2013**, *42*, 5880−5906.
(50) Godin, J.; Chen, C.-H.; Cho, S. H.; Qiao, W.; Tsai, F.; Lo, Y.-H. Microfluidics and Photonics for Bio-System-on-a-Chip: A Review of Advancements in Technology Towards A Microfluidic Flow Cytometry Chip. *J. Biophotonics* **2008**, *1*, 355−376.
(51) Han, D.; Fang, Y.; Du, D.; Huang, G.; Qiu, T.; Mei, Y. Automatic Molecular Collection and Detection by Using Fuel-powered microengines. *Nanoscale* **2016**, *8*, 9141−9145.
(52) Yin, Y.; Qiu, T.; Ma, L.; Lang, X.; Zhang, Y.; Huang, G.; Mei, Y.; Schmidt, O. G. Exploring Rolled-up Au-Ag Bimetallic Microtubes for Surface-Enhanced Raman Scattering Sensor. *J. Phys. Chem. C* **2012**, *116*, 25504−25508.
(53) Metzger, B.; Hentschel, M.; Schumacher, T.; Lippitz, M.; Ye, X.; Murray, C. B.; Knabe, B.; Buse, K.; Giessen, H. Doubling the Efficiency of Third Harmonic Generation by Positioning ITO Nanocrystals into the Hot-spot of Plasmonic Gap-Antennas. *Nano Lett.* **2014**, *14*, 2867−2872.
(54) Siegfried, T.; Ekinci, Y.; Martin, O. J. F.; Sigg, H. Gap Plasmons and Near-field Enhancement in Closely Packed Sub-10 nm Gap Resonators. *Nano Lett.* **2013**, *13*, 5449−5453.
(55) Pile, D. F. P.; Gramotnev, D. K. Channel Plasmon-polariton in A Triangular Groove on A Metal Surface. *Opt. Lett.* **2004**, *29*, 1069−1071.
(56) Chandrasekharan, N.; Kamat, P. V.; Hu, J.; Jones, G. Dye-Capped Gold Nanoclusters: Photoinduced Morphological Changes in

DOI: 10.1021/acsami.8b06962
ACS Appl. Mater. Interfaces 2018, 10, 25644−25651

Gold/Rhodamine 6G Nanoassemblies. *J. Phys. Chem. B* **2000**, *104*, 11103−11109.
(57) Wang, Y.; Yan, B.; Chen, L. SERS Tags: Novel Optical Nanoprobes for Bioanalysis. *Chem. Rev.* **2013**, *113*, 1391−1428.
(58) Qiu, T.; Zhang, W.; Lang, X.; Zhou, Y.; Cui, T.; Chu, P. K. Controlled Assembly of Highly Raman-enhancing Silver Nanocap Arrays Templated by Porous Anodic Alumina Membranes. *Small* **2009**, *5*, 2333−2337.
(59) Kim, M.-K.; Sim, H.; Yoon, S. J.; Gong, S.-H.; Ahn, C. W.; Cho, Y.-H.; Lee, Y.-H. Squeezing Photons into A Point-Like Space. *Nano Lett.* **2015**, *15*, 4102−4107.
(60) Rittersma, Z. M.; Splinter, A.; Bödecker, A.; Benecke, W. A Novel Surface-Micromachined Capacitive Porous Silicon Humidity Sensor. *Sens. Actuators, B* **2000**, *68*, 210−217.
(61) Jalkanen, T.; Mäkilä, E.; Määttänen, A.; Tuura, J.; Kaasalainen, M.; Lehto, V.-P.; Ihalainen, P.; Peltonen, J.; Salonen, J. Porous Silicon Micro- and Nanoparticles for Printed Humidity Sensors. *Appl. Phys. Lett.* **2012**, *101*, 263110.
(62) Ozdemir, S.; Gole, J. The Potential of Porous Silicon Gas Sensors. *Curr. Opin. Solid State Mater. Sci.* **2007**, *11*, 92−100.
(63) Christenson, H. K. Phase Behaviour in Slits-when Tight Cracks Stay Wet. *Colloid. Surfaces A* **1997**, *123-124*, 355−367.
(64) Yarom, M.; Marmur, A. Vapor-liquid Nucleation: the Solid Touch. *Adv. Colloid Interface Sci.* **2015**, *222*, 743−754.
(65) Yarom, M.; Marmur, A. Condensation Enhancement by Surface Porosity: Three-Stage Mechanism. *Langmuir* **2015**, *31*, 8852−8855.
(66) Ciccotti, M.; George, M.; Ranieri, V.; Wondraczek, L.; Marlière, C. Dynamic Condensation of Water at Crack Tips in Fused Silica Glass. *J. Non-Cryst. Solids* **2008**, *354*, 564−568.
(67) Maeda, N.; Israelachvili, J. N.; Kohonen, M. M. Evaporation and instabilities of microscopic capillary bridges. *Proc. Natl. Acad. Sci. U.S.A.* **2003**, *100*, 803−808.
(68) Zargarzadeh, L.; Elliott, J. A. W. Surface Thermodynamic Analysis of Fluid Confined in A Cone and Comparison with the Sphere-plate and Plate-plate Geometries. *Langmuir* **2013**, *29*, 12950−12958.
(69) Hong, S.; Yang, S.; Cho, S.; Jeon, H.; Lim, G. Development of a waterproof crack-based stretchable strain sensor based on PDMS shielding. *Sensors* **2018**, *18*, 1171.
(70) Late, D. J. Liquid Exfoliation of Black Phosphorus Nanosheets and its Application as Humidity Sensor. *Microporous Mesoporous Mater.* **2016**, *225*, 494−503.

DOI: 10.1021/acsami.8b06962
ACS Appl. Mater. Interfaces 2018, 10, 25644−25651